Available online at www.sciencedirect.com
ScienceDirect
Russian Geology and Geophysics 50 (2009) 475–484
RUSSIAN GEOLOGY AND GEOPHYSICS
www.elsevier.com/locate/rgg

Modeling electromagnetic field in shelf areas

A.V. Marinenko *, M.I. Epov, E.P. Shurina

Trofimuk Institute of Petroleum Geology and Geophysics, Siberian Branch of the RAS, 3 prosp. Akad. Koptyuga, Novosibirsk, 630090, Russia

Received 24 April 2008; accepted 24 September 2008

Abstract

Water salinity at shallow sea depths in shelf areas changes with depth, which causes respective conductivity changes. We discuss algorithms for computing monochromatic electric fields using the vector finite-element method with different realizations of depth dependence of conductivity. The algorithms have been applied to compute vertical conductivity patterns and to explore its influence on the electric field measured on the surface.

Keywords: marine geophysics; finite-element method; electric field; conductivity; electric charge

Introduction

Progress in marine geophysics is associated with the use of ever more sophisticated models in data processing. However, all models commonly assume invariable conductivity of sea water, though water at shallow sea depths in shelf areas is known to change in conductivity with depth as a result of salinity and temperature changes. The depth dependence of conductivity is specific to each area but is most often linear (Doronin, 1992; Egorov, 1974; Mikhailov, 1998; Mikhailov and Povalishnikova, 1999). See Fig. 1 for generalized salinity-conductivity relationships according to UNESCO data (The Practical Salinity Scale, 1981).

We explore the patterns of conductivity as a function of salinity and temperature using the example of the Black Sea. The water column in the Black Sea consists of two poorly mixing layers (Vershinin, 2007). The upper 100 m layer is fed from freshwater river input while the more saline and denser water below 100 m comes from the Sea of Marmara along the bottom of the Bosporus Strait (lower Bosporus current) and flows depthward. That is why the salinity of bottom water in the Black Sea reaches 30‰. Salinity and conductivity change in different ways with depth: salinity increases rapidly from 17 to 21‰ from the surface to 50–100 m, and conductivity first grows from ~1.75 to 2.1 S/m and then increases uniformly to 2.6 S/m as far as the bottom. In this study vertical conductivity patterns are investigated using the vector finite-element algorithms to simulate monochromatic electric fields.

Mathematical model

Maxwell's equations for the electromagnetic field are (Balandin and Shurina, 2001)

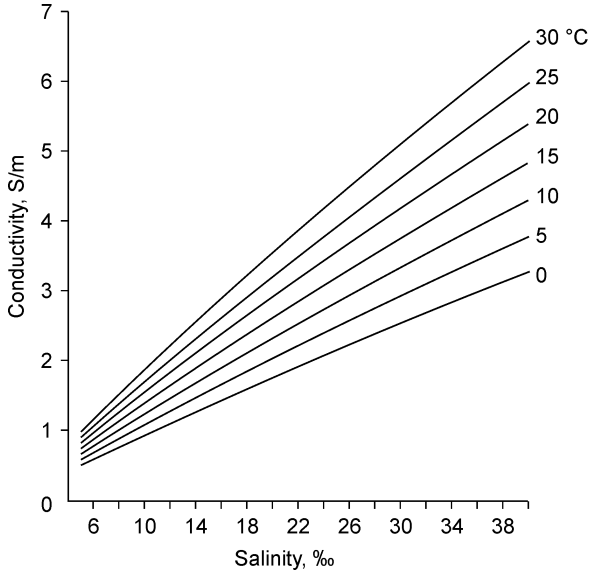

Fig. 1. Salinity and temperature dependences of seawater conductivity.

* Corresponding author.
E-mail address: arkadiy@reqip.net (A.V. Marinenko)

1068-7971/$ - see front matter © 2009, IGM, Siberian Branch of the RAS. Published by Elsevier B.V. All rights reserved.
doi:10.1016/j.rgg.2009.04.003

$$\begin{cases} \text{rot}\,\mathbf{E} = -\mu\dfrac{\partial \mathbf{H}}{\partial t}, \\ \text{rot}\,\mathbf{H} = \varepsilon\dfrac{\partial \mathbf{E}}{\partial t} + \sigma(x, y, z)\mathbf{E} + \mathbf{j}^e, \\ \text{div}(\mu\mathbf{H}) = 0, \\ \text{div}(\varepsilon\mathbf{E}) = \rho, \end{cases} \quad (1)$$

where **E** and *H* are the electric (V/m) and magnetic (A/m) fields, respectively, $\mathbf{j}^e$ is the eddy current density (A/m^2), ε is the permittivity (F/m), μ is the magnetic permeability (H/m), ρ is the charge density (C/m^3), $\sigma(x, y, z)$ is the conductivity (S/m), which is a function of space coordinates in the general case.

The second-order equation for the electric field vector **E** is

$$\text{rot}\frac{1}{\mu}\text{rot}\,\mathbf{E} = -\frac{\partial}{\partial t}\text{rot}\,\mathbf{H}\,.$$

Then, with regard to the second equation in system (1), it becomes

$$\text{rot}\frac{1}{\mu}\text{rot}\,\mathbf{E} = -\varepsilon\frac{\partial^2 \mathbf{E}}{\partial t^2} - \sigma(x, y, z)\frac{\partial \mathbf{E}}{\partial t} - \frac{\partial \mathbf{j}^e}{\partial t}.$$

Let $\mathbf{j}^e$ and **E** be expressed as

$$\mathbf{j}^e = \mathbf{j}^e e^{-i\omega t},$$

$$\mathbf{E} = \mathbf{E}e^{-i\omega t} = (\mathbf{E}^{re} + i\mathbf{E}^{im})e^{-i\omega t},$$

where *i* is an imaginary unit; superscripts *re* and *im* mark real and imaginary parts, respectively.

Thus, the behavior of the monochromatic electric field **E** in time domain is described by the Helmholz vector equation as

$$\text{rot}\frac{1}{\mu}\text{rot}\,\mathbf{E} - k^2\mathbf{E} = i\omega\mathbf{j}^e, \quad (2)$$

where $k^2 = i\omega\sigma(x, y, z) + \omega^2\varepsilon$ is the square wave number, and the real part of $\mathbf{j}^e$ is nonzero.

The law of free charge conservation is

$$\text{div}((\sigma + i\omega\varepsilon)\mathbf{E}) = 0. \quad (3)$$

We consider a problem with depth-dependent conductivity $\sigma = \sigma(z)$. In this case, the charge conservation law of (3) becomes

$$\frac{\partial\sigma(z)}{\partial z}E_z + (\sigma(z) + i\omega\varepsilon)\text{div}\mathbf{E} = 0. \quad (4)$$

If the electric field is generated by a current loop (induction source),

$$\text{div}(\mathbf{j}^e) = 0. \quad (5)$$

The first term in (4) corresponds to an additional charge due to depth-dependent conductivity change (the necessary condition for this is a nonzero *z* component of the electric field).

The conditions for continuity of the electric field **E** at the interfaces $\Gamma_{i,j}$ between different conductivity domains imply that $\Omega = \bigcup_i \Omega_i$, where each Ω_i has its own ε_i, μ_i, and σ_i and can be written as

$$[\mathbf{n}\times\mathbf{E}]_\Gamma = 0,$$

$$[\mathbf{n}\cdot(\sigma(z) + i\omega\varepsilon)\mathbf{E}]_\Gamma = 0.$$

The uniform boundary conditions at the interface are

$$\mathbf{n}\times\mathbf{E}\,|_{\partial\Omega} = 0.$$

Vector variation formulation

Let Ω be a three-dimensional physically inhomogeneous domain with the Lipshitz-continuous boundary ∂Ω. We introduce the Hilbert spaces

$$\mathbb{H}(\Omega) = \{\mathbf{v}|\mathbf{v} \in \mathbb{L}_2(\Omega)\},$$

where $\mathbb{L}_2(\Omega)$ is the space of the complex-valued or real functions integrated over the set Ω with the square

$$\mathbb{H}(\text{rot}; \Omega) = \{\mathbf{v}|\mathbf{v} \in \mathbb{H}(\Omega), \text{rot}\,\mathbf{v} \in \mathbb{H}(\Omega)\} \subset \mathbb{H}(\Omega),$$

$$\mathbb{H}_0(\text{rot}; \Omega) = \{\mathbf{v}|\mathbf{v} \in \mathbb{H}(\text{rot}; \Omega), \mathbf{n}\times\mathbf{v}|_{\partial\Omega} = 0\},$$

the norm

$$\|\mathbf{u}\|^2_{\text{rot},\,\Omega} = \int_\Omega \mathbf{u}\cdot\mathbf{u}^* d\Omega + \int_\Omega \text{rot}\,\mathbf{u}\cdot\text{rot}\,\mathbf{u}^* d\Omega$$

and the scalar product

$$(\mathbf{u}, \mathbf{v}) = \int_\Omega \mathbf{u}\cdot\mathbf{v} d\Omega.$$

The Galerkin variation formulation for (2) is to find $\mathbf{E} \in \mathbb{H}_0(\text{rot}; \Omega)$ such that for $\forall\mathbf{V}^* \in \mathbb{H}_0(\text{rot}; \Omega)$,

$$\left(\frac{1}{\mu}\text{rot}\,\mathbf{E}, \text{rot}\,\mathbf{V}^*\right) - (k^2\mathbf{E}, \mathbf{V}^*) = i(\omega\mathbf{j}^e, \mathbf{V}^*). \quad (6)$$

For the space $\mathbb{H}_0(\text{rot}; \Omega)$, there exists the embedding property that

$$\text{grad}\,\phi \in \mathbb{H}_0(\text{rot}; \Omega), \quad \forall\phi \in \mathbb{H}^1_0(\Omega). \quad (7)$$

According to (7) we may use $\text{grad}\,\phi$ for $\mathbf{V}^*$ where $\phi \in \mathbb{H}^1_0(\Omega)$. Then, (6) becomes

$$\left(\frac{1}{\mu}\text{rot}\,\mathbf{E}, \text{rot grad}\,\phi\right) - (k^2\mathbf{E}, \text{grad}\,\phi) =$$

$$i(\omega\mathbf{j}^e, \text{grad}\,\phi), \ \forall\phi \in \mathbb{H}^1(\Omega).$$

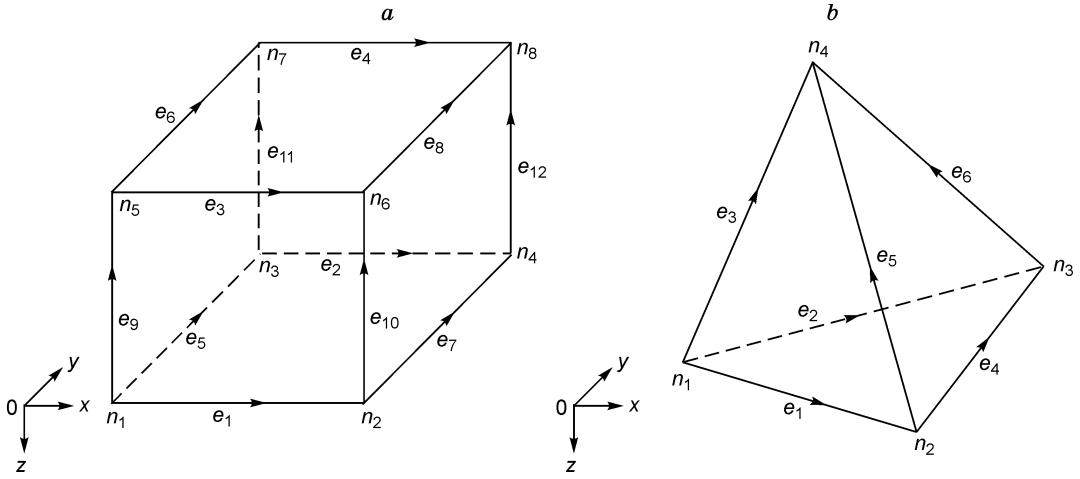

Fig. 2. Local numbering of edges (e_i) and vertices (n_j) of hexahedral (*a*) and tetrahedral (*b*) finite elements.

Taking into account (5) and zero rot grad ϕ,

$$((\omega^2\varepsilon + i\omega\sigma(z))\mathbf{E}, \operatorname{grad}\phi) = 0, \ \forall\phi \in \mathbb{H}^1(\Omega). \quad (8)$$

The scalar product of (3) and $\mathbf{V}^* = \operatorname{grad}\phi$ is

$$\int_\Omega (\omega^2\varepsilon + i\omega\sigma(z))\mathbf{E}\cdot\operatorname{grad}\phi \, d\Omega =$$

$$\int_\Omega \operatorname{div}[(\omega^2\varepsilon + i\omega\sigma(z))\mathbf{E}]\phi \, d\Omega, \quad (9)$$

where $\forall\phi \in \mathbb{H}_0^1(\Omega)$.

It follows from (9) that equation (8) is the variation equivalent of the conservation law of (4). Thus, the variation solution (6) satisfies the charge conservation law in weak sense.

Choice of finite elements and local vector basis functions

The model domain can be simulated by a hexahedral or a tetrahedral finite element mesh (Nechaev and Shurina, 2005), with basis edge functions in its cells associated with the edges of the mesh in the finite-dimension subspace $\mathbb{H}^h(\mathrm{rot};\Omega) \subset \mathbb{H}(\mathrm{rot};\Omega)$. The choice of hexahedral finite elements (Fig. 2, *a*) is optimum for domains of a simple geometry. The respective solutions with a well-structured hexahedral mesh can use basis functions of low orders, and iteration is of good convergence. However, domains of complex geometries require the use of deformed meshes (Solin, 2002) instead of the standard ones.

Below we consider both hexahedral and tetrahedral finite element meshes.

The hexahedral basis functions are obtained using the auxiliary functions

$$\psi_x^{\pm} = \frac{1}{l_x}\left(\frac{-}{+}\ x_c + \frac{l_x}{2} \pm x\right),$$

$$\psi_y^{\pm} = \frac{1}{l_y}\left(\frac{-}{+}\ y_c + \frac{l_y}{2} \pm y\right),$$

$$\psi_z^{\pm} = \frac{1}{l_z}\left(\frac{-}{+}\ z_c + \frac{l_z}{2} \pm z\right),$$

where $\{x_c, y_c, z_c\}$ is the center of the hexahedron and l_x, l_y, l_z are the lengths of its edges.

The hexahedral basis functions (space $\mathbb{H}^h(\mathrm{rot};\Omega);1)$) or first-order vector basis functions are

$$\mathbf{N}_1 = (\psi_y^- \psi_z^-)\mathbf{i},$$

$$\mathbf{N}_2 = (\psi_y^+ \psi_z^-)\mathbf{i},$$

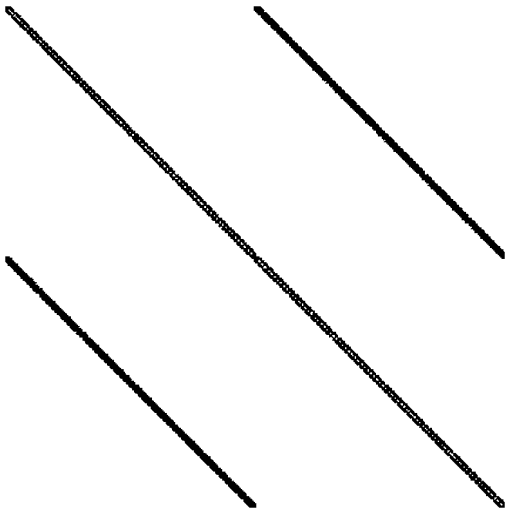

Fig. 3. Matrix for hexahedral mesh.

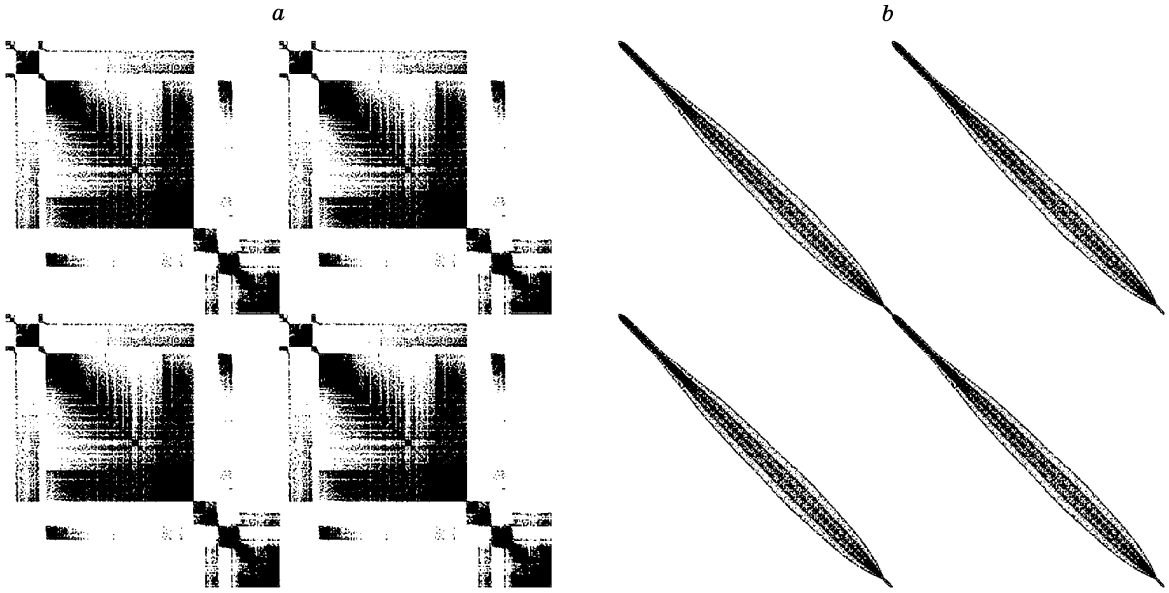

Fig. 4. Matrix for tetrahedral mesh, obtained without (*a*) and with (*b*) Cuthill–McKee algorithm.

$$\mathbf{N}_3 = (\psi_y^- \psi_z^+)\mathbf{i},$$

$$\mathbf{N}_4 = (\psi_y^+ \psi_z^+)\mathbf{i},$$

$$\mathbf{N}_5 = (\psi_x^- \psi_y^-)\mathbf{j},$$

$$\mathbf{N}_6 = (\psi_x^- \psi_z^+)\mathbf{j},$$

$$\mathbf{N}_7 = (\psi_x^+ \psi_z^-)\mathbf{j},$$

$$\mathbf{N}_8 = (\psi_x^+ \psi_z^+)\mathbf{j},$$

$$\mathbf{N}_9 = (\psi_x^- \psi_y^-)\mathbf{k},$$

$$\mathbf{N}_{10} = (\psi_x^+ \psi_y^-)\mathbf{k},$$

$$\mathbf{N}_{11} = (\psi_x^- \psi_y^+)\mathbf{k},$$

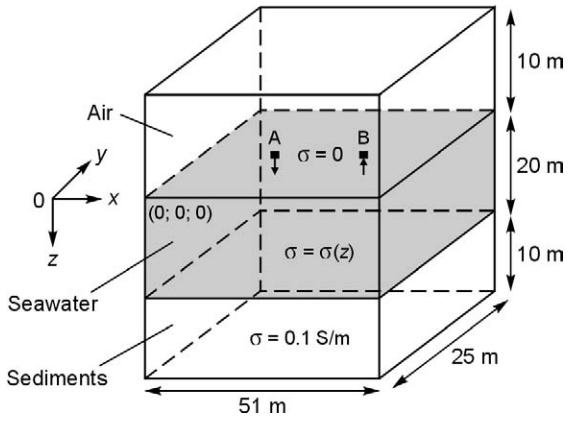

Fig. 5. Modeling layout.

$$\mathbf{N}_{12} = (\psi_x^+ \psi_y^+)\mathbf{k},$$

where **i**, **j**, **k** are the unit vectors in the Cartesian coordinates.

In tetrahedral meshes, the use of low-order basis functions cannot provide a satisfactory accuracy of the solutions. Then, we construct the hierarchic basis of the space $\mathbb{H}^h(\mathrm{rot}; \Omega; 2)$ (first-order vector basis functions of type 2) (Nechaev and Shurina, 2005):

$$\mathbf{W}_1 = \lambda_1 \nabla\lambda_2 - \lambda_2 \nabla\lambda_1,$$

$$\mathbf{W}_2 = \lambda_1 \nabla\lambda_3 - \lambda_3 \nabla\lambda_1,$$

$$\mathbf{W}_3 = \lambda_1 \nabla\lambda_4 - \lambda_4 \nabla\lambda_1,$$

$$\mathbf{W}_4 = \lambda_2 \nabla\lambda_3 - \lambda_3 \nabla\lambda_2,$$

$$\mathbf{W}_5 = \lambda_2 \nabla\lambda_4 - \lambda_4 \nabla\lambda_2,$$

$$\mathbf{W}_6 = \lambda_3 \nabla\lambda_4 - \lambda_4 \nabla\lambda_3,$$

$$\mathbf{W}_7 = \lambda_1 \nabla\lambda_2 + \lambda_2 \nabla\lambda_1,$$

$$\mathbf{W}_8 = \lambda_1 \nabla\lambda_3 + \lambda_3 \nabla\lambda_1,$$

$$\mathbf{W}_9 = \lambda_1 \nabla\lambda_4 + \lambda_4 \nabla\lambda_1,$$

$$\mathbf{W}_{10} = \lambda_2 \nabla\lambda_3 + \lambda_3 \nabla\lambda_2,$$

$$\mathbf{W}_{11} = \lambda_2 \nabla\lambda_4 + \lambda_4 \nabla\lambda_2,$$

$$\mathbf{W}_{12} = \lambda_3 \nabla\lambda_4 + \lambda_4 \nabla\lambda_3,$$

where λ_i are the 3D barycentric coordinates with respect to the vertices of the tetrahedron. The first six basis functions are associated with the tetrahedron edges and the other six functions are associated with their centers.

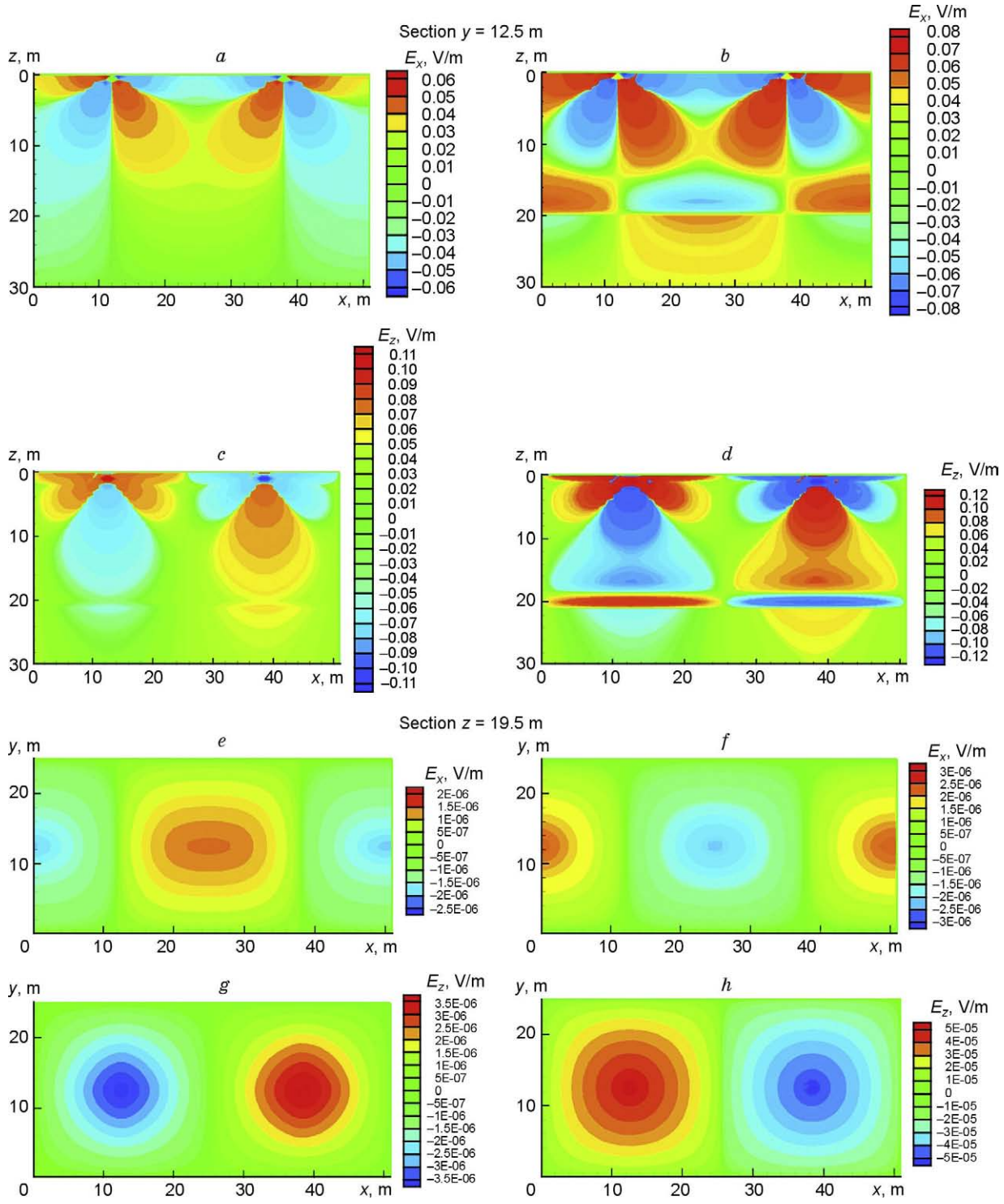

Fig. 6. Real part of electric field E_x (*a*, *b*, *e*, *f*); E_z (*c*, *d*, *g*, *h*). Seawater layer is assumed to have its conductivity uniform in *a*, *c*, *e*, *g* and gradient in *b*, *d*, *f*, *h*.

Discrete variation formulation

In the discrete variation formulation we approximate the elements of the space $\mathbb{H}(\mathrm{rot};\Omega)$ by elements of the discrete half-space $\mathbb{H}^h(\mathrm{rot};\Omega)$. Then, the discrete equivalent of (6) is

$$\left(\frac{1}{\mu}\mathrm{rot}\,\mathbf{E}_h^{re}, \mathrm{rot}\,\mathbf{V}_h^{1*}\right)_\Omega - \left(\omega^2\varepsilon\mathbf{E}_h^{re}, \mathbf{V}_h^{1*}\right)_\Omega +$$

$$\left(\omega\sigma(z)\mathbf{E}_h^{im}, \mathbf{V}_h^{1*}\right)_\Omega = 0,$$

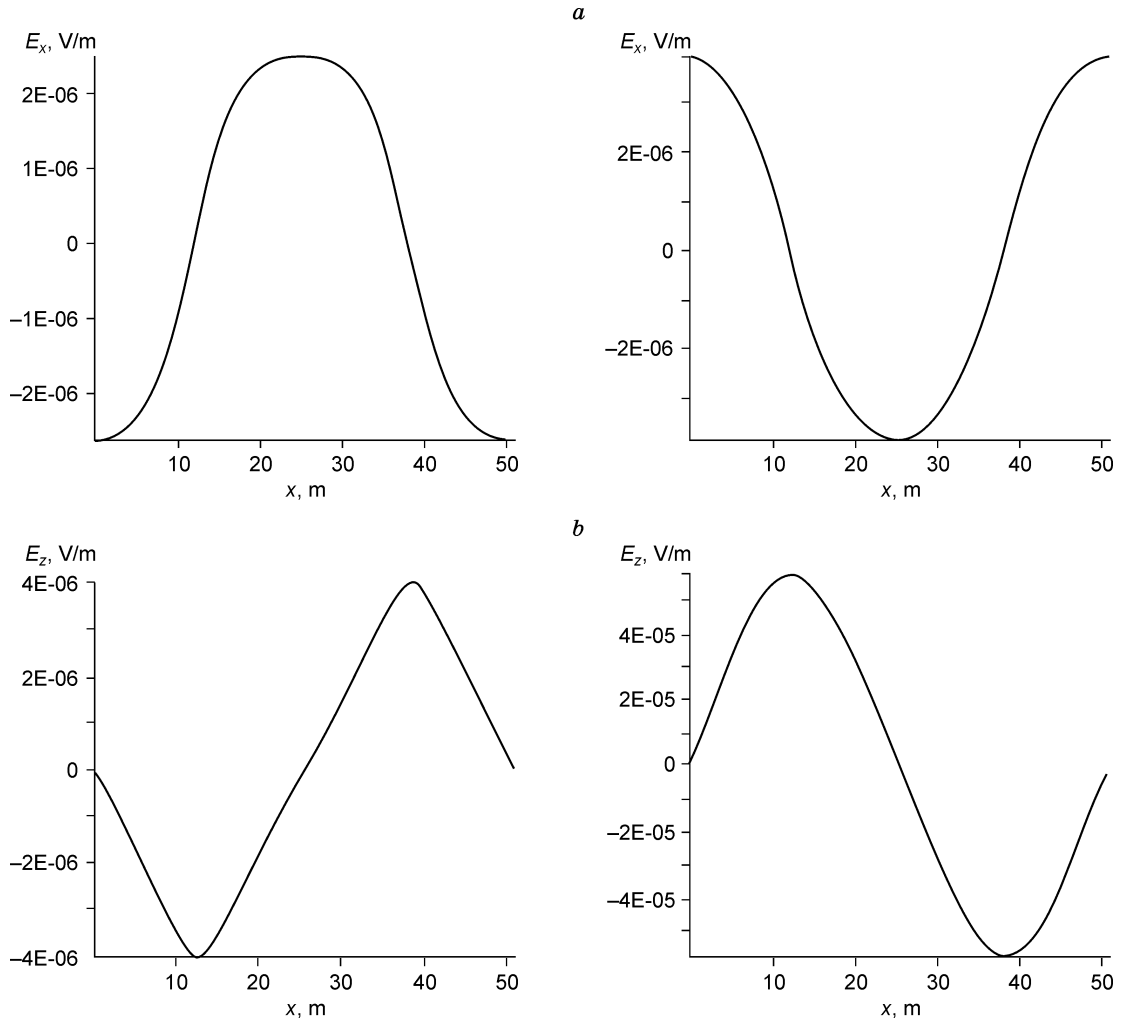

Fig. 7. Patterns of x (*a*) and z (*b*) components of electric field **E** in sections y = 12.5 m and z = 19.5 m.

$$\left(\frac{1}{\mu}\text{rot}\,\mathbf{E}_h^{im}, \text{rot}\,\mathbf{V}_h^{2*}\right)_\Omega - \left(\omega^2\varepsilon\mathbf{E}_h^{im}, \mathbf{V}_h^{2*}\right)_\Omega -$$

$$\left(\omega\sigma(z)\mathbf{E}_h^{re}, \mathbf{V}_h^{2*}\right)_\Omega = \left(\omega\mathbf{j}^e, \mathbf{V}_h^{2*}\right)_\Omega.$$

For the obtained discrete subspaces, there exists the embedding property that

$$\phi^h \in \mathbb{H}^h(\text{grad};\,\Omega) \to \text{grad}\phi^h \in \mathbb{H}^h(\text{rot};\,\Omega).$$

That is why the approximation of $\mathbf{E}_h$ satisfies the charge conservation law in weak sense:

$$(\omega\varepsilon\mathbf{E}_h^{re} - \sigma\mathbf{E}_h^{im}),\ \text{grad}\,\phi_h) = 0,\ \forall\phi^h \in \mathbb{H}_0^h(\text{grad};\,\Omega),$$

$$(-\omega\varepsilon\mathbf{E}_h^{om} - \sigma\mathbf{E}_h^{re}),\ \text{grad}\,\phi_h) = 0,\ \forall\phi^h \in \mathbb{H}_0^h(\text{grad};\,\Omega).$$

We are to find the solution in the subspace $\mathbb{H}_0^h(\text{rot};\,\Omega)$ for the real and imaginary parts of $\mathbf{E} = \mathbf{E}^{re} + i\mathbf{E}^{im}$. Written as a series with respect to all basis functions $\mathbf{N}_j \in \mathbb{H}_0^h(\text{rot};\,\Omega)$, they are

$$\mathbf{E}^{re} = \sum_j \alpha_j\mathbf{N}_j,\ \mathbf{E}^{im} = \sum_j \beta_j\mathbf{N}_j. \tag{10}$$

Thus the solution of variation problem (6) becomes equivalent to that with respect to the weights (α_j, β_j) in series (10)

$$\begin{pmatrix} \hat{A} + \hat{M}_\varepsilon & \hat{M}_\sigma \\ -\hat{M}_\sigma & \hat{A} + \hat{M}_\varepsilon \end{pmatrix} = \begin{pmatrix} \boldsymbol{\alpha} \\ \boldsymbol{\beta} \end{pmatrix} = \begin{pmatrix} 0 \\ \mathbf{F} \end{pmatrix}. \tag{11}$$

The elements of the matrices $\hat{A}$, $\hat{M}_\varepsilon$, $\hat{M}_\sigma$ and the vector **F** in the right-hand side of (11) are given by

$$\{\hat{A}\}_{ij} = \frac{1}{\mu}\int_\Omega \text{rot}\,\mathbf{N}_j\text{rot}\,\mathbf{N}_i\,d\Omega,$$

$$\{\hat{M}_\varepsilon\}_{ij} = -\omega^2\varepsilon\int_\Omega \mathbf{N}_j\mathbf{N}_i\,d\Omega,$$

$$\{\hat{M}_\sigma\}_{ij} = \omega\int_\Omega \sigma(z)\mathbf{N}_j\mathbf{N}_i\,d\Omega,$$

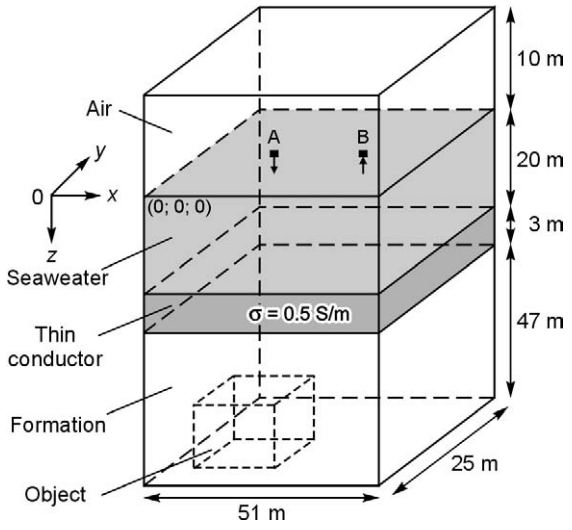

Fig. 8. Model including an embedded low-conductivity object.

$$\{\mathbf{F}\}_i = \omega \int_{\Omega} \mathbf{N}_i \mathbf{j}^e \, d\Omega.$$

The obtained system (11) of linear algebraic equations (SLAE) is asymmetrical. We tested several standard iteration methods for solving asymmetrical SLAE, such as BiCGStab (BiConjugate gradient Stabilized), CGS (Conjugate gradient Squared), TFQMR (Transpose Free Quasi-Minimal Residual), GMRES (Generalized Minimum Residual), and MGCR (Modified Generalized Conjugate Residual), and finally selected the GMRES method (Saad and Schultz, 1986) which showed the best efficiency. The SLAE matrix is well ordered for a hexahedral mesh (Fig. 3), but in the case of a non-structured tetrahedral mesh, the resulting matrix (distribution of nonzero elements) is strongly disordered (Fig. 4, *a*). We structured the SLAE matrix using a modified Cuthill–McKee (Cuthill and McKee, 1969) algorithm for tetrahedral mesh edge renumbering (Fig. 4, *b*). Inasmuch as attempts to speed up the computing process using standard preconditioning routines such as the Jacoby overrelaxation, SSOR (Symmetric Successive Overrelaxation), or ILU (Incomplete LU Factorization) had little effect, we applied iteration combined with the multiplicative Schwartz algorithm. For details see (Nechaev and Shurina, 2005).

Numerical modeling

We investigated the behavior of depth-dependent conductivity by simulating the monochromatic electric field in a domain consisting of three subdomains: air (vanishing conductivity), seawater (depth-dependent conductivity), and underlying sediments. See Fig. 5 for the sizes of the subdomains and the conductivity conditions.

Let the electric field be generated by a positive (A) and a negative (B) electrodes on the seawater surface, at a frequency of 100 Hz, with 1 A feeding current and the source electrodes spaced at 25 m, or slightly more than the sea depth.

The finite element mesh can be hexahedral or tetrahedral. In the latter case, where there are fewer edges, one can make the mesh denser in the regions where the field is strongly variable (near the sources) or sparser where the field is more stable (far from the sources). For instance, in the model of Fig. 5 the total number of edges was 320,866 for a hexahedral mesh and 156,705 (or about twice less) for a tetrahedral mesh. The tetrahedral mesh is commonly mirror symmetrical about the plane that divides in half the model domain along the x axis and is equidistant from the source electrodes, which is necessary for generating identical meshes in the case of geometrically identical sources.

Assume that in the Cartesian coordinates the plane *xOy* coincides with the sea surface and the *z* axis is directed downward.

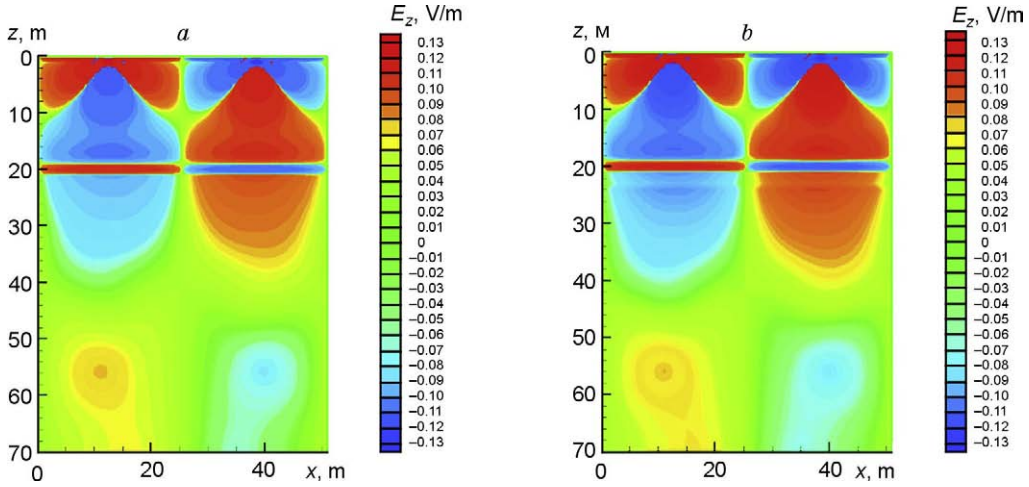

Fig. 9. Patterns of $\mathbf{E}_z^{re}$ component in section y = 12.5 m, without (*a*) and with (*b*) a thin conductor.

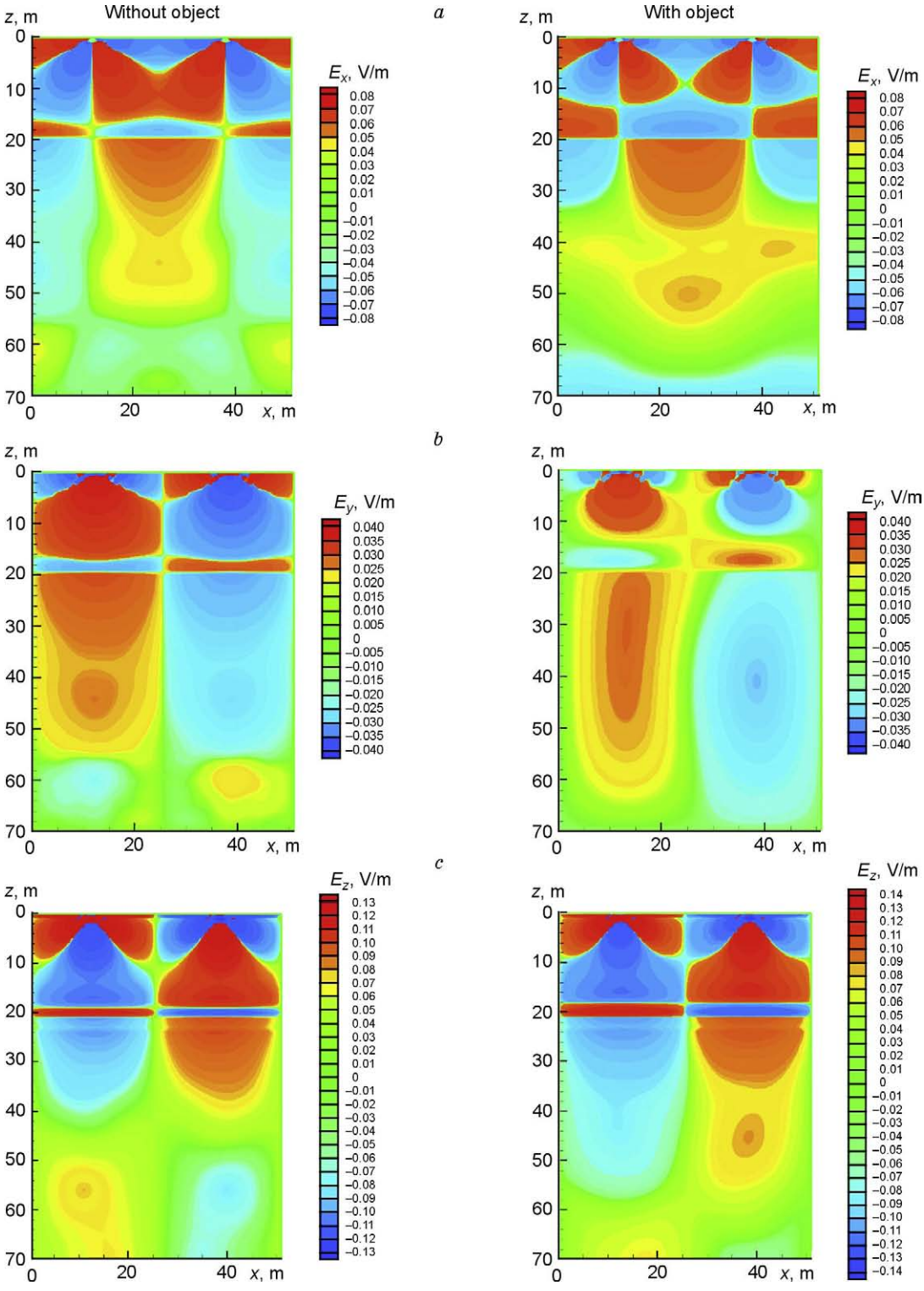

Fig. 10. Patterns of E_x^{re} (*a*), E_y^{re} (*b*), and E_z^{re} (*c*) components in section y = 12.5 m.

Forward modeling of marine resistivity survey data is commonly performed using layered models with constant depth-independent conductivities of seawater and other layers. This choice is due to (i) the existence of several workable forward methods for layered models and (ii) the impossibility to take into account all features of the conductivity pattern with a function dependence.

We assume the conductivity to be 5 S/m at the sea surface and 7 S/m near the bottom and the dependence $\sigma(z)$ to be linear:

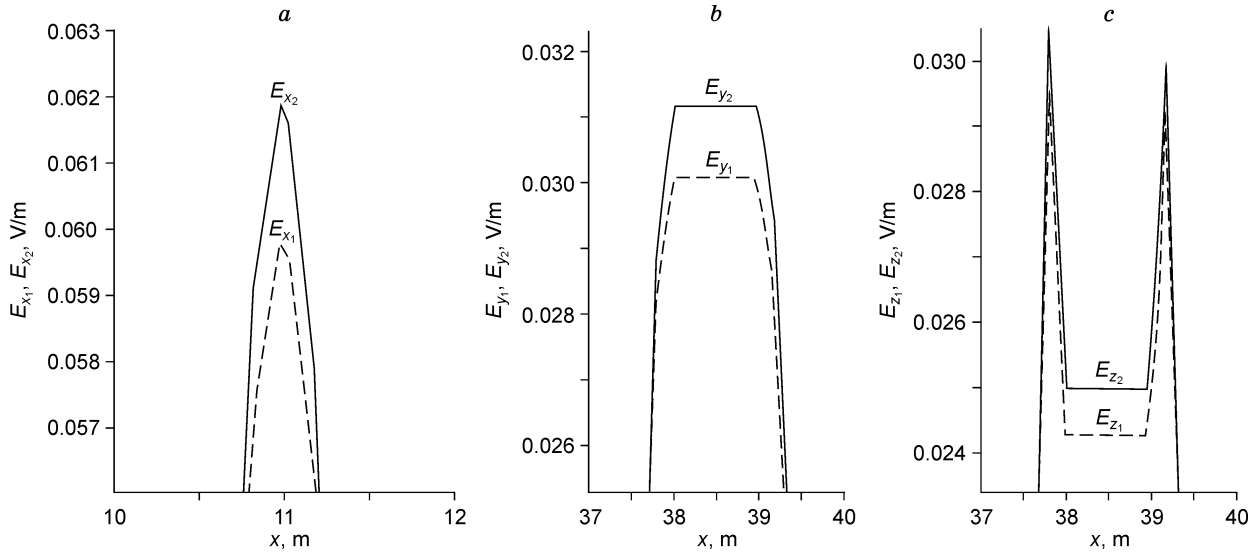

Fig. 11. Maximum E_x^{re} (*a*), E_y^{re} (*b*), and E_z^{re} (*c*) components in section y = 12.5 m, without (E_{x_1}, E_{y_1}, E_{z_1}) and with (E_{x_2}, E_{y_2}, E_{z_2}) embedded object.

$$\sigma(z) = \sigma_0\left(1 + \frac{z}{50}\right),$$

where $\sigma_0 = 5$ S/m.

Below we compare modeling results for two models, with the upper layer having either gradient depth-dependent or uniform conductivities (in the latter case the equivalent mean conductivity is $\sigma = 6$ S/m).

The images of Fig. 6 are for two real components of the electric field in the section y = 12.5 m (Fig. 6, *a–d*) and in the plane z = 19.5 m (Fig. 6, *e–h*) for the uniform (Fig. 6, *a*, *c*) and gradient (Fig. 6, *b*, *d*) conductivities of seawater.

The patterns for the horizontal field component agree well within the upper seawater layer, the difference being in a higher field intensity and a greater contrast between the positive and negative field parts in the gradient layer. The patterns for the bottom layer differ notably, mainly because there is a distributed charge in the gradient layer with the density $\delta \sim \frac{\partial \sigma}{\partial z} E_z$ which is absent from the layer of constant conductivity. Below the interface there is a compensating negative volumetric charge.

The orientation of curves in Fig. 7, *a*, *b* indicates the existence of a secondary source (a volumetric charge) in the gradient layer (near its bottom), the electrodes being the primary source. The distribution of volumetric sources at $\frac{\partial \sigma}{\partial z}$ showing low lateral variations depends on the distribution of the vertical field component, which is controlled, in turn, by the configuration of the source electrodes. Thus, by changing the configuration of source electrodes and their eddy currents one can manage the secondary sources that are located much closer to the study domain and have quite different geometric attenuation patterns.

Another numerical experiment was to investigate how a nonconducting object can influence the electric field and estimate the possibility for its detection from surface measurements.

Let a 10 m × 10 m × 10 m low-conductivity (σ = 0.01 S/m) cube be located at a depth of 50 m below the sea surface (Fig. 8). Its equidistant position from the sides of the model domain reduces the computational expenses but is almost never the case in reality. The electric field is measured at z_0 = 0.2 m below the sea surface.

First we compare the numerical results in models without perturbation consisting of two and three layers (without and with a thin conductor, respectively). The field components E_x^{re}, E_y^{re}, and E_z^{re} are very similar in this case, but differ at greater depth, especially in $\mathbf{E}_z^{re}$ (Fig. 9). Thus, the effect of a thin conductor cannot be neglected.

Figure 10 shows distortions of different field components ($\mathbf{E}^{re}$), with and without the embedded object, and the surface field changes caused by the object (Fig. 11).

The presence of a low-conductivity object obviously influences the $\mathbf{E}_{\text{pattern}}^{re}$ (see the antisymmetry disappearing on the left and on the right of the plane x = 25.5 m) and, moreover, shows up as increase in all three field components measured on the surface (Figs. 10 and 11).

Conclusions

We performed numerical experiments for seawater with conductivities assumed either to be a constant mean or to change linearly with depth. The use of algorithms that account for depth dependence of conductivity indicated the presence of volumetric charges at the interface between the seawater and the underlying rocks. The results may be useful in developing new processing methods marine resistivity survey data.

References

Balandin, M.Yu., Shurina, E.P., 2001. The Vector Finite-Element Method [in Russian]. NGTU, Novosibirsk.

Cuthill, E., McKee, J., 1969. Reducing the bandwidth of sparse symmetric matrices, in: Proc. 24th Nat. Conf. ACM, pp. 157–172.

Doronin, Yu.P., 1992. Modeling the vertical pattern of a river mouth with a marine halocline. Meteorologiya i Gidrologiya, No. 8, 76–83.

Egorov, N.I., 1974. Physical Oceanography [in Russian] Gidrometeoizdat, Leningrad.

Mikhailov, V.N., 1998. Hydrology of River Deltas [in Russian]. Moscow University Press, Moscow.

Mikhailov, V.N., Povalishnikova, E.S., 1999. Hydrology of Seas. Learner's Guide [in Russian]. Moscow University Press, Moscow.

Nechaev, O.V., Shurina, E.P., 2005. A multigrid algorithm for solving the Helmholtz equation by the vector finite-element method. Matematicheskoe Modelirovanie 17 (6), 92–102.

Saad, Y., Schultz, M.H., 1986. GMRES: a generalized minimal residual algorithm for solving non-symmetric linear systems. J. of Scientific Statistical Computing 7, 856–869.

Solin, P., 2002. Scalar and Vector-Valued Finite Elements of Variable Order. TICAM Report 02-36. The University of Texas, Austin.

The Practical Salinity Scale 1978 and the International Equation of State of Seawater 1980, 1981. UNESCO Technical Papers in Marine Science 36. Paris.

Vershinin, A.O., 2007. The Life of the Black Sea [in Russian]. Kogorta, Krasnodar–Moscow.

Editorial responsibility: V.S. Seleznev